Effect of Porosity, Thickness and Tortuosity on Capacity Fade of Anode

Bharatkumar Suthar,[a],* Paul W. C. Northrop,[b], Derek Rife,[a],***
and Venkat R. Subramanian[c],[d],,[z]**

[a]*Department of Energy, Environmental & Chemical Engineering, Washington University, St. Louis, Missouri 63130, USA*
[b]*CFD Research Corporation, Biomedical and Energy Technologies, Huntsville, Alabama 35806, USA*
[c]*Department of Chemical Engineering, Clean Energy Institute, University of Washington, Seattle, Washington 98195, USA*
[d]*Energy Processes and Materials Department, Pacific Northwest National Laboratory, Richland, Washington 99354, USA*

The graphite anode in lithium-ion batteries is vulnerable to capacity fade due to several mechanisms. Advancement in understanding of such capacity fade mechanisms has paved the way for selecting design parameters that consider these effects. This paper shows the effect of porosity, thickness, and tortuosity of the anode on capacity fade mechanisms. Three main capacity fade mechanisms are analyzed in this paper: (1) solid electrolyte interface (SEI) side reaction, (2) lithium plating side reactions and (3) mechanical degradation due to intercalation induced stresses. Moreover, for a given thickness and porosity of anode, the effect of porosity variation on capacity fade mechanisms is also presented.

Lithium-ion chemistries are attractive for many applications due to high cell voltage, high volumetric and gravimetric energy density (100 Wh/kg), high power density (300 W/kg), good temperature range, low memory effect, and relatively long battery life.[1–3] Capacity fade, underutilization, and thermal runaway are the main issues that need to be addressed in order to use a lithium-ion battery efficiently and safely over a long life.

Research on various fronts is underway to address the issues mentioned above. While finding better materials and improving their properties is one approach, the use of system level strategies to reach better efficiency in existing and emerging systems is another approach. The true potential of battery materials cannot be realized due to system level efficiencies, especially where transport effects become dominant (e.g. higher rates of charging/discharging at normal temperature or low temperatures operations).

One of the many problems that can be addressed by continuum level modeling approaches is finding the optimum thicknesses and porosities of anode and cathode materials while keeping various processes and objectives in mind. These objectives may be discharge capacities at higher rates, charging time, mechanical degradation due to intercalation induced stresses, loss of active lithium due to parasitic side reaction (SEI layer and lithium plating), safety etc. While one would like to maximize energy density by packing the solid phase material compactly with larger thickness; rate capacity, safety and capacity fade may cause such an approach to be impractical.

How should one choose the porosity and length of anode and cathode is an interesting research problem. Design optimization (porosity and thickness) for lithium-ion battery can be traced back to the work done by Prof. Newman using the reaction zone model[4] and with the pseudo two dimensional model.[5] Work on determining the optimal porosity distribution by considering the ohmic drop has been done by Ramadesigan et al.[6] Effect of low temperature and porosity on the performance of lithium-ion batteries is also studied by Ji et al.[7] While these works are based on maximizing the energy/power density of lithium-ion batteries by choosing optimal design parameters, no work has been done in quantifying the effect of design parameters on capacity fade mechanisms. With the advances made in understanding

capacity fade reactions and intercalation induced stresses in intercalation materials, proper treatment can be given in selection of the porosity and the thicknesses of electrode materials based on detailed electrochemical engineering models augmented with capacity fade mechanisms.

One of the practical problems that can be addressed by continuum level models can be summarized in a question: "*How should one choose the design parameters (thicknesses, porosities, area etc) so that high rate capacity and energy density can be achieved considering the effect of capacity fade mechanisms?*". Although this is a problem of practical importance, the large number of design parameters prevent a full understanding to be developed here. Rather, we choose a simpler problem of selecting the porosity and thickness of the anode and their effect on capacity fade mechanisms, while maintaining all other parameters constant.

Model description section briefly introduces the continuum level model used to simulate battery charge/discharge behavior and explains intercalation induced stress and overpotentials for parasitic side reactions. Problem statement section describes the problem statement of selecting design parameters for improved battery design. Results and discussion section discusses simulation results which highlight the effect of porosity and length of the anode as well as porosity variation in anode on capacity fade and cell capacities, followed by conclusion.

Model Description

Detailed models that incorporate electrochemical, transport, and thermodynamic processes along with the geometry of the underlying system can be used to monitor and control the internal states of a battery.[8] The isothermal porous electrode pseudo-two dimensional (P2D) model is one such model which is given in Table I. Table II presents various expressions used in this model. The P2D model is general enough to incorporate various capacity fade mechanisms. This paper focuses on three main sources of capacity fade and safety issues in batteries: intercalation induced stresses, SEI layer side reaction and lithium plating side reaction.

Intercalation induced stresses.— Various models, varying in their sophistication, have been proposed to quantify the intercalation-induced stresses in the solid particles. These models are divided in two categories: stress splitting[9,10] and strain splitting.[11–13] In this

*Electrochemical Society Student Member.
**Electrochemical Society Active Member.
[z]E-mail: vsubram@uw.edu

Table I. Governing PDEs for the P2D model.

Governing Equations	Boundary Conditions
Positive Electrode	
$\varepsilon_p \frac{\partial c}{\partial t} = \frac{\partial}{\partial x}\left[D_{\text{eff},p}\frac{\partial c}{\partial x}\right] + a_p(1-t_+)j_p$	$\frac{\partial c}{\partial x}\big|_{x=0} = 0$
	$-D_{\text{eff},p}\frac{\partial c}{\partial x}\big|_{x=l_p^-} = -D_{\text{eff},s}\frac{\partial c}{\partial x}\big|_{x=l_p^+}$
$-\sigma_{eff,p}\frac{\partial \Phi_1}{\partial x} - \kappa_{\text{eff},p}\frac{\partial \Phi_2}{\partial x} + \frac{2\kappa_{\text{eff},p}RT}{F}(1-t_+)\frac{\partial \ln c}{\partial x} = I$	$\frac{\partial \Phi_2}{\partial x}\big|_{x=0} = 0$
	$-\kappa_{\text{eff},p}\frac{\partial \Phi_2}{\partial x}\big|_{x=l_p^-} = -\kappa_{\text{eff},s}\frac{\partial \Phi_2}{\partial x}\big|_{x=l_p^+}$
$\frac{\partial}{\partial x}\left[\sigma_{\text{eff},p}\frac{\partial \Phi_1}{\partial x}\right] = a_p F j_p$	$\sigma_{eff,p}\frac{\partial \Phi_1}{\partial x}\big|_{x=0} = -I$
	$\frac{\partial \Phi_1}{\partial x}\big|_{x=l_p^-} = 0$
$\frac{\partial c_p^s}{\partial t} = \frac{1}{r^2}\frac{\partial}{\partial r}\left[r^2 D_p^s \frac{\partial c_p^s}{\partial r}\right]$	$\frac{\partial c_p^s}{\partial r}\big|_{r=0} = 0, \ D_p^s \frac{\partial c_p^s}{\partial r}\big|_{r=R_{P,p}} = -j_p$
Separator	
$\varepsilon_s \frac{\partial c}{\partial t} = \frac{\partial}{\partial x}\left[D_{\text{eff},s}\frac{\partial c}{\partial x}\right]$	$c\big|_{x=l_p^-} = c\big|_{x=l_p^+}$
	$c\big|_{x=l_p+l_s^-} = c\big|_{x=l_p+l_s^+}$
$-\kappa_{\text{eff},s}\frac{\partial \Phi_2}{\partial x} + \frac{2\kappa_{\text{eff},s}RT}{F}(1-t_+)\frac{\partial \ln c}{\partial x} = I$	$\Phi_2\big|_{x=l_p^-} = \Phi_2\big|_{x=l_p^+}$
	$\Phi_2\big|_{x=l_p+l_s^-} = \Phi_2\big|_{x=l_p+l_s^+}$
Negative Electrode	
$\varepsilon_n \frac{\partial c}{\partial t} = \frac{\partial}{\partial x}\left[D_{\text{eff},n}\frac{\partial c}{\partial x}\right] + a_n(1-t_+)j_n$	$\frac{\partial c}{\partial x}\big|_{x=l_p+l_s+l_n} = 0$
	$-D_{\text{eff},s}\frac{\partial c}{\partial x}\big|_{x=l_p+l_s^-} = -D_{\text{eff},n}\frac{\partial c}{\partial x}\big|_{x=l_p+l_s^+}$
$-\sigma_{\text{eff},n}\frac{\partial \Phi_1}{\partial x} - \kappa_{\text{eff},n}\frac{\partial \Phi_2}{\partial x} + \frac{2\kappa_{\text{eff},n}RT}{F}(1-t_+)\frac{\partial \ln c}{\partial x} = I$	$\Phi_2\big|_{x=l_p+l_s+l_n} = 0$
	$-\kappa_{\text{eff},s}\frac{\partial \Phi_2}{\partial x}\big|_{x=l_p+l_s^-} = -\kappa_{\text{eff},p}\frac{\partial \Phi_2}{\partial x}\big|_{x=l_p+l_s^+}$
$\frac{\partial}{\partial x}\left[\sigma_{\text{eff},n}\frac{\partial \Phi_1}{\partial x}\right] = a_n F j_n$	$\frac{\partial \Phi_1}{\partial x}\big|_{x=l_p+l_s^+} = 0$
	$\sigma_{eff,n}\frac{\partial \Phi_1}{\partial x}\big|_{x=l_p+l_s+l_n} = -I$
$\frac{\partial c_n^s}{\partial t} = \frac{1}{r^2}\frac{\partial}{\partial r}\left[r^2 D_n^s \frac{\partial c_n^s}{\partial r}\right]$	$\frac{\partial c_n^s}{\partial r}\big|_{r=0} = 0, \ D_n^s \frac{\partial c_n^s}{\partial r}\big|_{r=R_{P,n}} = -j_n$

paper, a model presented by Cheng and Verbrugge[11] is used. This stress model does not incorporate a moving boundary formulation and ignores thermodynamic factors and pressure-induced diffusion. These simplifications restrict its use to materials with very low volumetric expansion. The resulting equations describing radial stress (σ_r) and tangential stress (σ_t) generated in spherical particles are given in Table III. Dimensionless radial ($\overline{\sigma}_r$) and tangential stresses ($\overline{\sigma}_t$) as

defined in Table III are plotted throughout this paper. Also, tensile stress is taken as positive and compressive stress is taken as negative. Here Ω_n is the partial molar volume of the solute, E_n is the Young's modulus, and ν_n is the Poisson's ratio. Parameters values used in this paper are listed in Table IV.

During intercalation, for the materials with a positive volume expansion, the radial stresses remain tensile throughout a particle (as-

Table II. Additional expressions used in the P2D model.

$$j_p = 2k_p c^{0.5} c^s\big|_{r=R_{P,p}}{}^{0.5} (c_{\max,p}^s - c^s\big|_{r=R_{P,p}})^{0.5} \sinh\left[\frac{F}{2RT}(\Phi_1 - \Phi_2 - U_p)\right]$$

$$j_n = 2k_n c^{0.5} c^s\big|_{r=R_{P,n}}{}^{0.5} (c_{\max,n}^s - c^s\big|_{r=R_{P,n}})^{0.5} \sinh\left[\frac{F}{2RT}(\Phi_1 - \Phi_2 - U_n)\right]$$

$$\kappa_{eff,i} = \varepsilon_i^{bruggi} \times 10^{-4} c \left(\begin{matrix} -10.5 + 0.074T - 6.96\times10^{-5}T^2 + 6.68\times10^{-4}c - \\ 1.78\times10^{-5}cT + 2.8\times10^{-8}cT^2 + 4.94\times10^{-7}c^2 - 8.86\times10^{-10}Tc^2 \end{matrix} \right)^2, i = p, s, n$$

$$\sigma_{eff,i} = \sigma_i(1 - \varepsilon_i - \varepsilon_{f,i}), i = p, s, n$$

$$D = 2.33\times10^{-4} \times 10^{-4.43 - \frac{54}{(T-5\times10^{-3}c - 229)} - 2.2\times10^{-4}c}$$

$$D_{eff,i} = D\varepsilon_i^{bruggi}, i = p, s, n$$

$$a_i = \frac{3}{R_i}(1 - \varepsilon_i - \varepsilon_{f,i}), i = p, s, n$$

$$U_p = \frac{-4.656 + 88.669\theta_p^2 - 401.119\theta_p^4 + 342.909\theta_p^6 - 462.471\theta_p^8 + 433.434\theta_p^{10}}{-1.0 + 18.933\theta_p^2 - 79.532\theta_p^4 + 37.311\theta_p^6 - 73.083\theta_p^8 + 95.96\theta_p^{10}}$$

$$\theta_p = \frac{c^s\big|_{r=R_{P,p}}}{c_{p,\max}^s}; 0.4955 \le \theta_p \le 0.99$$

$$U_n = -0.057 + 0.53e^{-57\theta} - 0.184\tanh(20.0\theta - 21.0) - 0.012\tanh(7.57\theta - 4.431)$$
$$-0.0304\tanh(18.518\theta - 3.24) - 0.01\tanh(0.255\theta - 0.02653)$$

$$\theta_n = \frac{c^s\big|_{r=R_{P,n}}}{c_{n,\max}^s} 0.01 \le \theta_n \le 0.99$$

$$D_i^s = D_{i,0}^s e^{\left(-\frac{E_i^{D^s}}{R}\left(\frac{1}{T} - \frac{1}{T_{ref}}\right)\right)}, i = p, n$$

$$k_i = k_{i,0} e^{\left(-\frac{E_i^k}{R}\left(\frac{1}{T} - \frac{1}{T_{ref}}\right)\right)}, i = p, n$$

Table III. Governing equations for intercalation-induced stress.

Governing Equation

$$\overline{\sigma}_r(\xi, t) = \frac{3\sigma_r(\xi,t)}{\left(\frac{\Omega_n E_n c_{n,\max}^s}{(1-\nu_n)}\right)} = \frac{2}{3}\left(\int_0^1 \frac{c_n^s(\xi,t)}{c_{n,\max}^s}\xi^2 d\xi - \frac{1}{\xi^3}\int_0^\xi \frac{c_n^s(\xi,t)}{c_{n,\max}^s}\xi^2 d\xi\right)$$

$$\overline{\sigma}_t(\xi, t) = \frac{3\sigma_t(\xi,t)}{\left(\frac{\Omega_n E_n c_{n,\max}^s}{(1-\nu_n)}\right)} = \left(2\int_0^1 \frac{c_n^s(\xi,t)}{c_{n,\max}^s}\xi^2 d\xi + \frac{1}{\xi^3}\int_0^\xi \frac{c_n^s(\xi,t)}{c_{n,\max}^s}\xi^2 d\xi - \frac{c_n^s(\xi,t)}{c_{n,\max}^s}\right)$$

suming zero external pressure at the surface) whereas the tangential stress becomes compressive at the surface and tensile at the center. The peak (tensile) radial stress occurs at the center of the particle and peak (compressive) tangential stress occurs at the surface of the particle.[9] During deintercalation, the nature of stresses changes (i.e. tensile stresses become compressive and compressive stresses become tensile), but the location of peak stresses remains the same for both. Therefore, the peak radial stresses at the center of the particles and peak tangential stresses at the surface of the particles are monitored. As shown by Christensen and Newman[9] and also clear from the equations given in Table III, the peak tangential stresses and the peak radial stresses are same at the center of the particles, and so monitoring one of the either stresses would be sufficient for our analysis.

Due to the finite thickness of the anode, the pore wall flux becomes non-uniform except at very small rates of charging and discharging. This non uniformity of the pore wall flux changes with time as well. In general, the pore wall flux is higher at the anode separator interface at the onset of charge/discharge of the battery; afterwards, the pore wall flux decreases at the anode-separator interface and increases at the anode-current collector interface. Due to the time-varying and thickness-dependent non-uniformity of the pore wall flux, different maximum peak stresses are observed at different times during charge/discharge. Usually, the anode-separator interface faces largest pore wall flux resulting in maximum peak stresses at that point compared to other locations of the anode. Figure 1 shows the
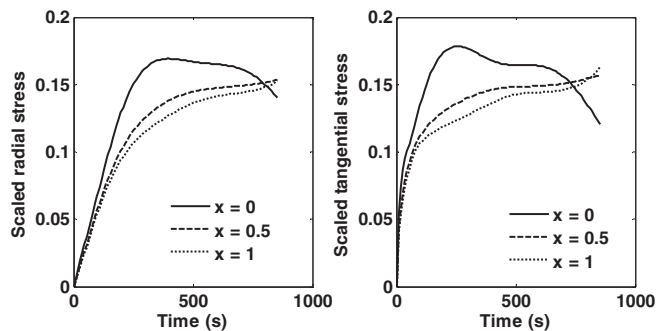

Figure 1. Distribution of radial and tangential stresses (dimensionless) during charging at 4C at 25°C ($x = 0$ represent anode-separator interface and $x = 1$ represent anode-current collector interface).

distribution of peak radial ($\overline{\sigma}_r$) and tangential stresses ($\overline{\sigma}_t$) at different locations in anode with time. In this paper, we will focus on peak stresses and their maximum values in the solid particle at the anode-separator interface (solid curves in Figure 1). One more thing to note here is that the dynamics of peak tangential stresses (which occurs at the surface) is faster compared to peak radial stresses (which occurs at the center).

Lithium plating side reaction.— As mentioned earlier, lithium plating side reaction not only causes capacity fade but also poses a significant safety issue.[14] Though lithium-ion batteries are inherently safer than lithium-metal batteries, as the former avoids dendrite formation during charging, the slightly more positive potential of LiC_6 compared to Li/Li^+ inherits the problem of lithium plating during charging[14] at high rates and even low rates at low temperature (0.2 C at −20°C).[15,16]

The driving force for the partially irreversible[16] lithium plating side reaction at the anode can be expressed by the over-potential:[17]

$$\eta_{plating}(x, t) = \Phi_1(x, t) - \Phi_2(x, t) - U_{plating,n} \qquad [1]$$

Table IV. List and values of parameters.

Symbol	Parameter	Positive Electrode[a]	Separator[a]	Negative Electrode[a]	Units
$Brugg$	Bruggeman coefficient	1.5 /2.5	1.5 [b]	1.5 [b]	
$c_{i,\max}^s$	Maximum solid phase concentration	51554		30555	mol/m³
c_0	Initial electrolyte concentration	1000	1000	1000	mol/m³
$D_{i,o}^s$	Reference solid phase diffusivity	1×10^{-14}		3.9×10^{-14}	m²/s
$E_i^{D^s}$	Activation energy for diffusivity	5000 [b]		5000 [b]	J/mol
E_i^k	Activation energy for reaction rate	5000 [b]		5000 [b]	J/mol
F	Faraday's constant		96487		C/mol
$k_{i,o}$	Reference reaction rate constant	2.33×10^{-11}		5.03×10^{-11}	m$^{2.5}$/(mol$^{0.5}$ s)
l_i	Region thickness	80×10^{-6}	25×10^{-6}	88×10^{-6}	m
$R_{p,i}$	Particle radius	2×10^{-6} [b]		10×10^{-6} [b]	m
R	Gas constant		8.314		J/mol/ K
T_{ref}	Temperature		298.15		K
t_+	Transference number		0.364		
$\varepsilon_{f,i}$	Filler fraction	0.025		0.0326	
ε_i	Porosity	0.385	0.724	0.485	
ρ	Density	2500	1100	2500	kg/m³
σ_i	Solid phase electronic conductivity	59		48.24	S/m
Ω	Partial molar volume	4.0815×10^{-6} [c]			m³/mol
E	Young's modulus	15×10^9 [d]			Pa
ν	Poisson's ratio	0.3 [d]			
$\Re_{SEI}$	Resistance	0.00215 [b]			Ω
ρ_e	Density of electrolyte	2000 [b]			kg/m³

[a]Unless otherwise noted, all parameters used for the electrodes and separator are from Ref. 27 Porosity, length, surface area for anode is given for base case.
[b]Assumed value.
[c]Values obtained from Renganathan et al.[13]
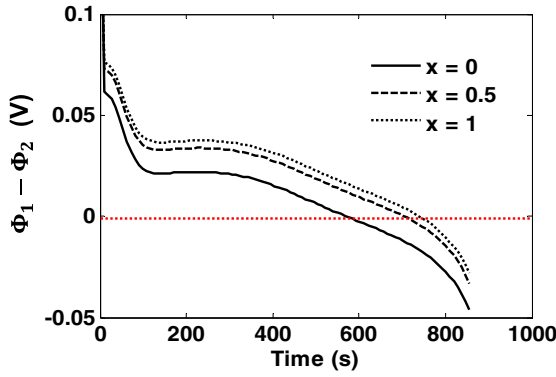[d]Values obtained from Christensen et al.[28]

Figure 2. Distribution of over-potential for lithium plating side reaction across length during charging at 4C rate ($x = 0$ represent anode-separator interface and $x = 1$ represent anode-current collector interface).
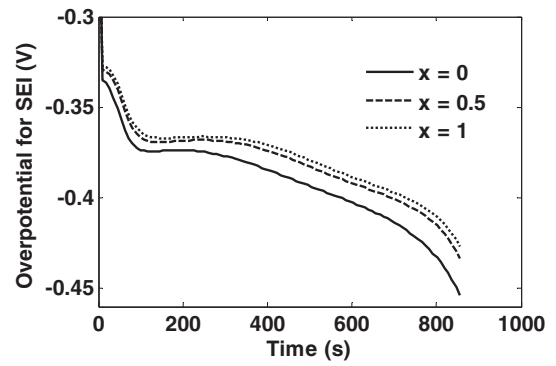

Figure 3. Distribution of over-potential for SEI side reaction across length during charging at 4C rate ($x = 0$ represent anode-separator interface and $x = 1$ represent anode-current collector interface).

where $\eta_{plating}$ is the over-potential for lithium plating side reaction, Φ_1 is the solid phase potential in negative electrode, Φ_2 is the electrolyte-phase potential in anode, $U_{plating,n}$ is the open-circuit potential for the plating reaction which is taken to be zero, and x is the distance across the electrode. The expression for $\eta_{plating}$ given in Eq. 1 ignores the voltage drop across the solid electrolyte interface (SEI) layer. For a uniform porosity anode, the anode-separator interface becomes most vulnerable to plating side reaction. Figure 2 shows the typical evolution of $\Phi_1(x, t) - \Phi_2(x, t)$ during charging.

Only when $\Phi_1(x, t) - \Phi_2(x, t)$ is less than zero, the plating reaction is favored. Figure 2 shows that at anode-separator interface, the plating side reaction becomes feasible sooner and achieves larger magnitude compared to other parts of the anode.

Over-potential for SEI layer.— In this simulation the voltage drop across the SEI layer is not modeled in the rigorous sense given in Equation 2,[18]

$$\eta_{SEI}(x, t) = \Phi_1(x, t) - \Phi_2(x, t) - U_{SEI}$$
$$- \left(\frac{\delta(x, t)}{\kappa_{SEI}} + \Re_{SEI}\right)(j_{SEI}(x, t) + j_n(x, t)) F \quad [2]$$

Here, $\Re_{SEI}$ is the resistance of SEI layer formed during the initial cycles and $\delta(x, t)/\kappa_{SEI}$ refers to the increase in resistance during the fresh buildup of SEI layer. Simplified expression given in Equation 3 is used to approximate the over-potential for SEI layer assuming that the increase in SEI layer thickness is very small per cycle. In our opinion this is justified as the magnitude of voltage drop across the SEI layer and current density associated with SEI layer ($j_{SEI}(x, t)$) are small, hence Equation 3 should give a good approximation to Equation 2 for any reasonable operation.

$$\eta_{SEI}(x, t) = \Phi_1(x, t) - \Phi_2(x, t) - U_{SEI} - \Re_{SEI} j_n(x, t) F \quad [3]$$

Figure 3 shows the evolution of overpotential for SEI layer as approximated by Equation 3. Here also, the magnitude is larger for anode-separator interface and hence will be the focus of this study.

Problem Statement

While various factors (thicknesses of electrodes and current collector, particle radius, filler fractions, porosity etc.) can be varied to get the optimal battery design, here we focus on the porosity and length of anode and its effect on battery performance. The porous solid phase structure in the anode and cathode consists of networks of interconnected and irregular pores or channels. Usually the electrode materials are designed as porous structures made up of solid particles. One way to reduce the complexity of these structures and avoid pore scale modeling is to use macro homogeneous models[8] where tortuosity is used to obtain effective transport properties.[19,20] A

Bruggeman relationship is often used to relate tortuosity τ with porosity as $\varepsilon^{1-brugg_n}$ where $brugg_n$ is the Bruggeman coefficient. Effective conductivity and diffusivity in the porous anode can be expressed as follows:

$$\kappa_{eff,n} = \frac{\kappa \varepsilon_n}{\tau} = \varepsilon_n^{brugg_n} \kappa \quad [4]$$

$$D_{eff,n} = \frac{D \varepsilon_n}{\tau} = D \varepsilon_n^{brugg_n} \quad [5]$$

Here κ (S/m) and D (m^2/s) are intrinsic conductivity and diffusivity of the electrolyte, and both are function of lithium ion concentration and temperature, whereas $\kappa_{eff,n}$ and $D_{eff,n}$ are the effective conductivity and diffusivity taking the porous nature into account. The increase in porosity would improve the conductivity and diffusivity of lithium-ions in the electrolyte. The solid phase conductivity is given in Equation 6, which denotes the porosity correction of the intrinsic conductivity of solid phase material.

$$\sigma_{eff,n} = \sigma_n \left(1 - \varepsilon_n - \varepsilon_{f,n}\right) \quad [6]$$

here σ_n and $\sigma_{eff,n}$ are the intrinsic electronic conductivity (S/m) and the effective electronic conductivity of solid phase of anode respectively. As porosity increases, the electronic conductivity will decrease as less volume is available for charge transport in the solid phase.

Assuming spherical shape and uniform particle size, the specific area can also be written as follows:

$$a_n = \frac{3}{R_{P,n}} \left(1 - \varepsilon_n - \varepsilon_{f,n}\right) \quad [7]$$

a_n is the specific area (m^2/m^3) and, $R_{P,n}$ is radius of anode particles and $\varepsilon_{f,n}$ is filler fraction. An increase in porosity will lead to a decrease in area. In this study, two scenarios are analyzed with respect to discharge capacity and effect on capacity fade mechanisms during both charge and discharge.

- Varying porosity and length with fixed total capacity
- Varying porosity across thickness for fixed length and average porosity

Varying porosity and length with fixed total capacity.— As mentioned before, the problem treated in this work assumes a given loading of the anode and cathode material. We allow the variation of length and porosity such that the total capacity of anode remains constant. In other words, choice of low porosity will lead to smaller thickness of anode and high porosity will lead to larger thickness of anode. Figure 4 illustrates the same.

Table V shows the capacity of cathode and anode as well as initial concentration for discharge simulation. For safety and capacity fade related issues, the anode is not allowed to be completely discharged or completely charged.
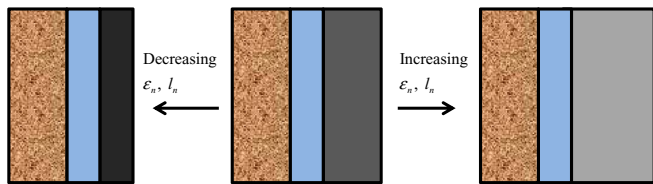
Figure 4. Different choices of porosities and lengths for fixed anode capacity.

Figure 5. Linear porosity distribution in anode.

The problem at hand is to vary porosity and length such that the material loading in anode remains the same, i.e.,

$$\left(1 - \varepsilon_{n,new} - \varepsilon_{fn}\right) l_{n,new} = \left(1 - \varepsilon_n - \varepsilon_{fn}\right) l_n \qquad [8]$$

Base values of anode length (l_n) and porosity (ε_n) are taken as 88×10^{-6} m and 0.485 respectively which corresponds to anode capacity given in Table V. Different thicknesses ($l_{n,new}$) and porosities ($\varepsilon_{n,new}$) will be chosen based on the constraint given by Equation 8.

The maximum theoretical capacity of the battery will be determined by the smaller of the capacities of two electrodes. Depending on the initial lithium concentration in anode and cathode, the maximum theoretical capacity of battery will differ. Initial concentration and corresponding capacities of the base case undertaken are listed in Table V. List of porosities and corresponding lengths constrained by Equation 8 used in this study are given in Table VI. Note that some of the porosity values may not be experimentally feasible due to negligible mechanical strength of highly porous electrode[21] (i.e. porosity 0.55). Filler fraction is also assumed to be the same for all the porosity and length combination. The electrodes with smaller porosity and thickness are referred to as *thinner-less porous* electrodes and electrodes with larger porosity and thickness are referred as *thicker-more porous* electrodes.

Varying porosity across thickness for fixed average porosity and length.— The second scenario considered in this study tries to quantify the effect of inhomogeneity of porosity in a given electrode. It has been shown by Chen et al.[22] that electrodes are not uniform in porosity distribution and contain patches of small and large porosities due to manufacturing limitations. In this scenario, one such example of varying porosity and its effect on capacity fade mechanics is studied. The problem statement is simplified by taking a linearly varying porosity distribution of the form given in Equation 9.

$$\varepsilon_n(x) = \varepsilon_{avg,n} + s\left(x - \frac{1}{2}\right) \qquad [9]$$

Here $\varepsilon_{avg,n}$ is the average porosity of the anode, s is the slope of porosity distribution, and x represents the scaled thickness of the anode which goes from 0 (anode-separator interface) to 1 (anode-current collector interface). This form of porosity variation across anode will make sure that the average porosity remains the same which in turn will ensure that the material loading does not vary when the porosity distribution is changed (see Figure 5). To see the effect of local porosity variation on side reactions, we choose the anode thickness to be 63.9×10^{-6} m and average porosity to be $\varepsilon_{avg,n} = 0.30$.
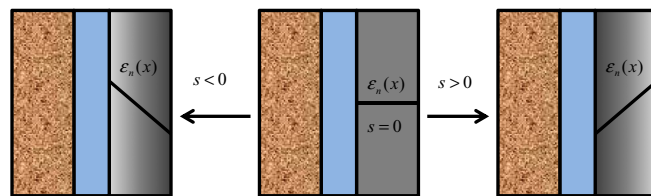
For the case when s is negative, the anode-separator interface has maximum porosity and anode-current collector has least porosity. On the other hand when s is positive, the reverse is true. Then case when s is positive could be understood by assuming a patch of low porosity at the anode-separator interface.

Results and Discussion

Battery charge and discharge are simulated at isothermal conditions. A voltage cutoff of 2.8 V is used for discharging and 4.2 V is used for charging. The following definitions of energy and average power density are used.

$$\text{Energy density} \equiv 1/m_{cell} \int_0^{t_f} V(t) I_{app} dt$$

$$\text{Average power density} \equiv 1/(t_f m_{cell}) \int_0^{t_f} V(t) I_{app} dt$$

where m_{cell} is the mass of the cell sandwich per unit area (only accounts for the mass of the electrodes, electrolyte and separator; mass of the current collectors and other accessories are not used in this calculation). t_f is the final time when the cell reaches 2.8 V while discharging, and I_{app} is the applied current (A/m^2). Since the energy density and power density used here excludes the contribution from current collector and other accessories, a factor of 0.33 may be used to estimate the capacity of entire cell.[5] For scenarios mentioned previously, different values of Bruggeman coefficient and temperature are used, resulting in three cases: 1) $brugg_n$ 1.5, T 298 K, 2) $brugg_n$ 2.5, T 298 K, 3) $brugg_n$ 1.5, Low temperature (288 K for discharge and 278 K for Charge). The Ragone plots are generated with discharge current up to 14C rate. Higher discharge current and lower temperature leads to very high electrolyte concentration in the *thinner- less porous* electrode configurations (> 4000 mol/m^3) for which the expression for concentration dependent intrinsic conductivity and diffusivity are not applicable. This is why during discharge a temperature of 288 K is used for simulation but during charging (where only 4C rate is considered), a lower temperature of 278 K is used.

Varying porosity and length with fixed total capacity.— During discharging, the effect of length-porosity is analyzed for battery capacities (Ragone plots) and intercalation-induced stresses. The effect of length-porosity on parasitic side reactions (plating and SEI reactions) in the anode is only relevant during charging hence their effect is studied during charging alone.

Table V. Capacities and initial concentration (charged condition) of both electrodes.

Electrode	Initial concentration	Capacity of electrodes	
Cathode	$c_{p,0}^s = 0.5 c_{p,max}^s$	$(1 - \varepsilon_p - \varepsilon_{fp}) l_p (c_{p,0}^s - c_{p,min}^s)$	1.217 mol/m^2
Anode	$c_{n,0}^s = 0.95 c_{n,max}^s$	$(1 - \varepsilon_n - \varepsilon_{fn}) l_n (c_{n,max}^s - c_{n,0}^s)$	1.232 mol/m^2

Table VI. List of porosities and lengths used.

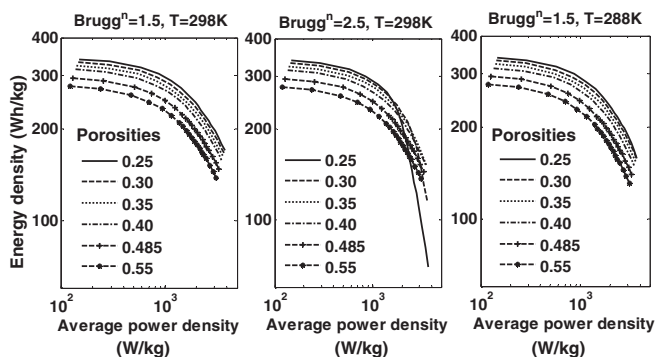| Length $l_{n,new}$(m)	59.5×10^{-6}	63.9×10^{-6}	69×10^{-6}	75×10^{-6}	88×10^{-6}	101.4×10^{-6}
Porosity $\varepsilon_{n,new}$	0.25	0.30	0.35	0.40	0.485	0.55

Figure 6. Simulated Ragone plot for different porosity-thickness combinations of anode (note that these energy and power densities are based on mass of electrolyte, electrode and separator only).

Figure 8. Maximum peak radial stresses during discharging at different C rates.

Discharging: Ragone plots and intercalation-induced stresses.—For the given initial conditions and cell parameters, the discharge curves were simulated at different rates and Ragone plots were generated for all six combinations of length-porosity given in Table VI (Figure 6). It is to be noted that difference in energy density at lower power density is strictly due to the change in the weight of the electrolyte in the anode as the weight of the solid phase of the anode is constant for every choice of length and porosity. The time to reach 2.8 V (t_f) at low rate of discharge is almost equal for all porosity-length choices (which is expected).

The simulated points in Figure 6 show the effect of length and porosity on battery performance. For a smaller Bruggeman coefficient ($brugg_n = 1.5$) the *thinner-less porous* electrodes give rise to higher energy density even at low temperature of 278 K due to less electrolyte weight (left and right subplots of Figure 6). At very high rates of discharge, the final time (t_f) starts to shrink down for the *thinner-less porous* electrodes compared to the *thicker-more porous* electrodes but less electrolyte weight in the *thinner-less porous* still dominates the energy density.

The Bruggeman coefficient value is usually taken as 1.5 for porous structures made by uniform size spherical particles.[19,23] For other shapes and variation in particle size, higher values of Bruggeman coefficient can be used. As can be seen from Figure 6 (middle subplot), the discharge capacity for the *thinner-less porous* electrodes at high power density decreases significantly when the Bruggeman coefficient is higher. In other words, t_f for the *thinner-less porous* electrodes is very short at higher discharge rates as compared to the *thicker-more porous* electrodes.

During deintercalation, the peak radial stresses are compressive at the center and peak tangential stresses are tensile at the surface. Figure 7 and Figure 8 show the extremum values obtained for peak tangential stresses (surface of the particle) and peak radial stresses (center of the particle) in the solid particle at the anode-separator interface during the discharge period. As mentioned before, the anode-separator in-
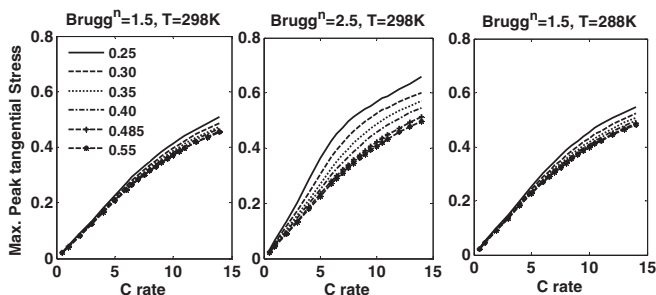
terface is most likely to face the largest magnitude of stresses during charging/discharging (Figure 1). For case 1 (*brugg_n* 1.5, room temperature, left subplots of Figure 7 and Figure 8) maxima for each type of peak stresses increases monotonically with the discharge rate. For the *thinner-less porous* electrodes, the maximum values for both radial and tangential stresses are higher compared to the *thicker-more porous* electrodes. At low temperature (case 3, right subplots), the maximum value of peak tangential stresses reaches higher values compared to room temperature case. On the other hand, the maximum values achieved by radial stresses seem to decrease at higher discharge rates. This apparent decrease happens simply because the cell does not last long enough for radial stresses to reach their maximum (as mentioned earlier, the peak radial stresses have slower dynamics, see Figure 1).
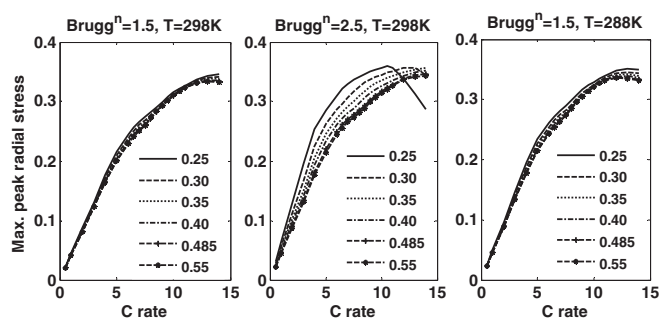
For higher Bruggeman coefficients, the *thinner-less porous* electrodes lead to significant increase in maximum values of both peak tangential stresses and peak radial stresses. For the *thinner-less porous* electrode, the maximum value of peak radial stresses decreases at higher rate of discharge because the t_f is not long enough for radial stresses to reach their maximum. It is clear that the *thinner-less porous* electrodes with smaller porosities lead to higher stresses in the particle and the stress effect becomes critical if the anode tortuosity is higher. It is worth mentioning here that for few cases for the *thinner-less porous* electrodes with high Bruggeman coefficients, the electrolyte concentration at the very end of discharge shoots up to as high as 5 molar (note that the diffusivity and conductivity expressions used here may not be very accurate). This is the reason why temperature lower than 288 K is not used for discharge simulation.

Charging: Intercalation-induced stresses.—The anode is vulnerable to parasitic side reactions (SEI layer and plating side reaction) during charging. The intercalation induced stresses during charging are also studied here although Takahashi and Srinivasan[24] suggest that fracture during lithiation is not likely. Initial anode concentration 961 mol/m^3 and initial cathode concentration 51022 mol/m^3 is used to simulate the battery charging.

Here, a charging rate of 4C is used to analyze the battery performance. The effective resistance during charging and discharging are different due to the asymmetrical nature of open circuit potentials of anode and cathode. Unlike the case for discharge, here we focus on only 4C rate of charging to illustrate the capacity fade mechanics during charging. During discharging, the final time to reach 2.8 V at 4C rate is almost same for all the cases (around 10 s difference between the *thinner-less porous* and the *thicker-more porous* electrodes for *brugg_n* 2.5 and *T* 298 K), but during charging, the time to reach 4.2 V is significantly different especially for higher Bruggeman coefficient (a difference of 200 s for *brugg_n* 2.5 and *T* 298 K). For the charging rate of 4C for different cases, Figure 9 shows voltage profile and effect of length-porosity combination on final time to reach 4.2 V. For the *thinner-less porous* anodes, the charging capacity drops down significantly for the higher Bruggeman coefficient.

During charging, the effect of porosity-length combination on the peak radial and peak tangential stresses is shown in Figure 10 and
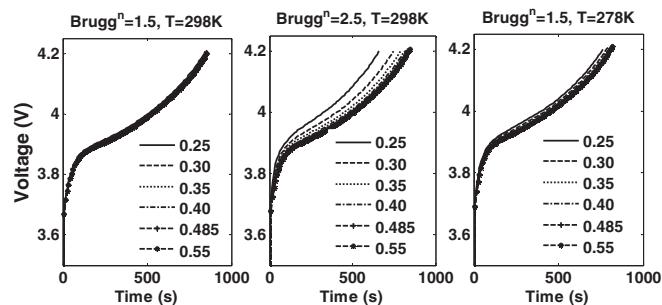

Figure 7. Maximum peak tangential stresses during discharging at different C rates.

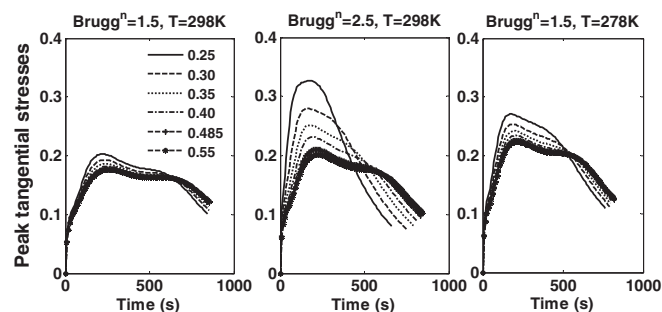**Figure 9.** Voltage profiles during charging at 4C rate for different anode thicknesses.

Figure 10. Peak tangential stresses (compressive) at anode-separator interface during charging at 4C rate.

Figure 11. Peak tangential stress (at the surface of the solid particle) is now compressive and peak radial stress (at the center of the particle) is tensile. Figure 10 shows the peak tangential stress at the surface of the solid particle at anode-separator interface. Since, only a single charging rate is used here (4C rate), time evolution of stress profiles are plotted for different thickness-porosity combinations unlike the discharging case (Figure 7 and Figure 8) where only the maximum values of these peak stresses are plotted. Figure 11 show peak radial stresses and at the anode-separator interface. Both peak radial and peak tangential stresses at anode-separator interface go through maxima during charging at 4C. The porosity-length combination has significant effect on the extremum values reached by peak radial and tangential stresses. For the *thicker-more porous* anode, the stress values remain similar as can be seen from Figure 10 and Figure 11 (curves for the *thicker-more porous* electrodes are virtually indistinguishable), but for the *thinner-less porous* anode peak stresses are significantly higher at higher Bruggeman coefficient (around 50% increase!).

Charging: Parasitic reactions.—The anode-separator interface remains the most vulnerable part of the battery with respect to parasitic side reactions (see Figure 2 for distribution of over-potential with
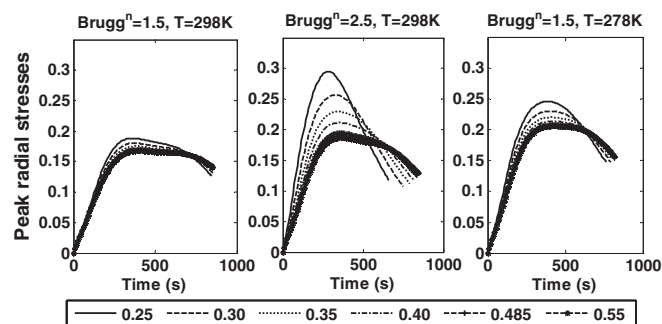

Figure 11. Peak radial stresses (tensile) at anode-separator interface during charging at 4C rate.
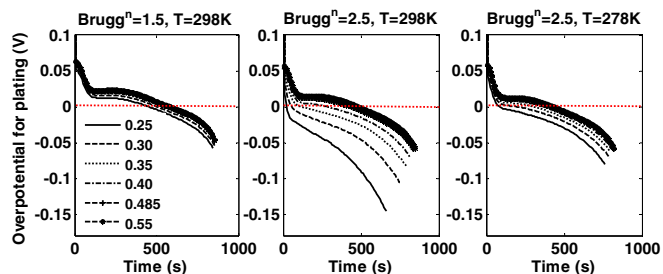

Figure 12. Over-potential for plating side reaction during charging at 4C rate (note that plating reaction in feasible only when over-potential is negative).

anode thickness), Figure 12 shows the over-potential for plating at anode-separator interface. As mentioned earlier, the plating side reaction becomes feasible only when the over-potential is negative. Similar to previous cases, the over-potential for plating reaction is higher for the *thinner-less porous* electrode irrespective of the Bruggeman coefficient and temperature. The effect is more severe with a higher Bruggeman coefficient (middle subplot, Figure 12). Lower temperature with smaller Bruggeman coefficient (i.e. 1.5) does lead to higher driving force for plating side reaction.

Similarly, the over-potential for the SEI side reaction is plotted in Figure 13. The SEI side reaction is irreversible and becomes feasible only during intercalation in anode. The over-potential for SEI reaction follows the similar trends as over-potential for plating side reactions. For the *thinner-less porous* anode, over-potential for SEI side reactions is higher compared to other cases, and for higher Bruggeman coefficient, the effect is more pronounced. It should be mentioned here that the current density for both the SEI side reaction and the lithium plating reaction has exponential dependence on the overpotentials.

Varying porosity across thickness for fixed average porosity and length.— Due to manufacturing limitations, the electrode structure may not have a uniform porosity distribution. In order to mimic the inhomogeneity of porosity in simplest fashion, a linear varying porosity is assumed. Three values of slopes (0.2, 0 and –0.2) are used to carry out simulation with average porosity ($\varepsilon_{avg,n}$) of 0.30 and thickness of 63.9×10^{-6} m (Table VI, case 2). Steeper porosity distribution ($|s| > 0.2$) lead to very small porosities at either end or causes electrolyte concentration to shoot up significantly above 4 molar during the end of charge/discharge.

Discharging: Ragone plots and intercalation-induced stresses.—Figure 14 shows the simulate Ragone plot for different porosity gradient. Since the average porosity is constant ($\varepsilon_{avg,n} = 0.30$) for all the cases, the energy and power densities are identical at very small rate of discharge. Even at higher rates of discharge, smaller Bruggemann coefficient ($brugg_n = 1.5$) does not lead to much change in energy density. On the other hand, higher Bruggeman coefficient with positive slope of 0.2 (less porosity at the anode-separator interface) leads to significant reduction in discharge capacity. Though the discharge capacities are not much affected by the porosity gradients for a smaller
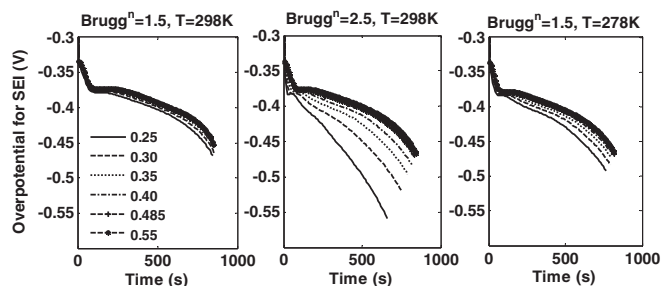

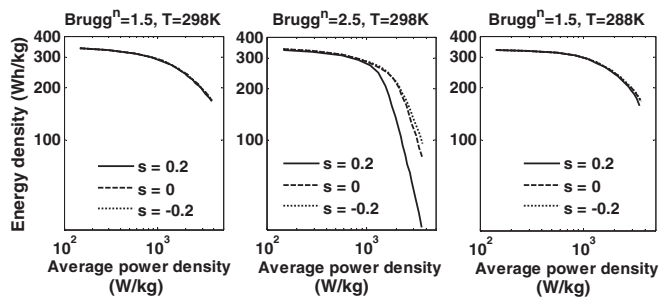**Figure 13.** Over-potential for SEI side-reaction during charging at 4C rate.

Figure 14. Simulated Ragone plot for different porosity gradient of anode (note that these energy and power densities are based on mass of electrolyte, electrode and separator only).
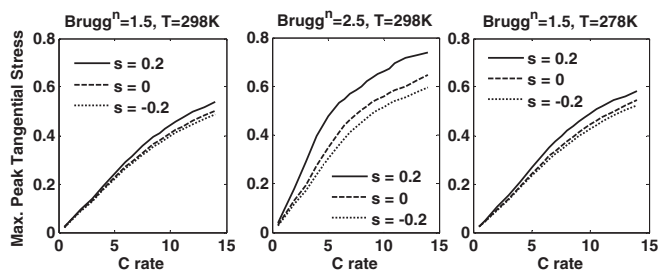

Figure 15. Maximum peak tangential stresses during discharging at different C rates.

Bruggeman coefficient, the maximum peak tangential stresses (tensile during deintercalation) at the anode-separator interface are influenced by the gradients (see Figure 15). Maximum peak radial stresses also follow trends similar to the maximum peak tangential stresses, except at the high discharge rates for higher Bruggeman coefficient where battery voltage drops below 2.8 V before the peak radial stresses could reach their maxima (middle subplot of Figure 16). Negative slope of −0.2 (more porosity at anode-separator interface) gives rise to better capacity and less stresses compared to zero and positive porosity gradient. Similar to the previous scenario of discharging, the electrolyte concentration shoots above 5 molar concentration near the end of discharge for a very few cases for higher Bruggeman coefficient.

Charging: Intercalation-induced stresses.—Figure 17 shows the charging profiles with porosity gradient. In each case the voltage rise is faster when slope is positive. Here also, in each case, negative porosity gradient (more porosity at anode-separator interface) gives favorable capacity fade behavior compared to zero and positive slope. Positive porosity gradient turns out to be very critical for higher Bruggeman coefficient (middle subplots).

Figure 18 and Figure 19 shows the peak radial (tensile) and peak tangential (compressive) stresses respectively.

Charging: Parasitic reactions.—Figure 20 and Figure 21 shows the overpotential for SEI and plating side reactions. These curves also
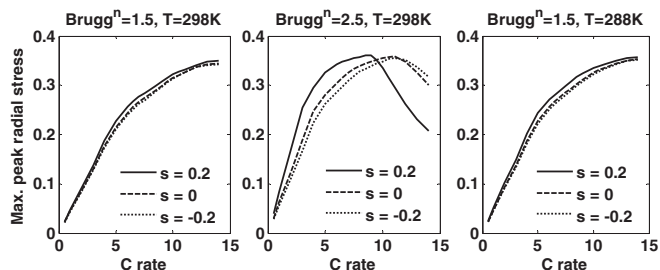

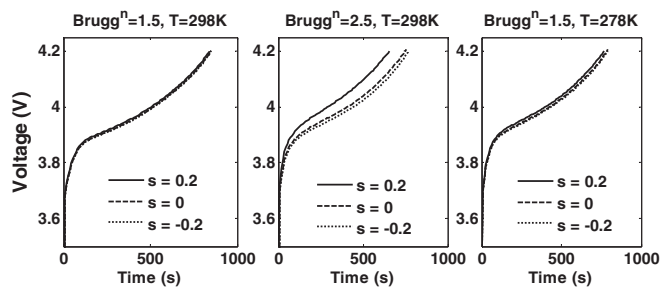**Figure 16.** Maximum peak radial stresses during discharging at different C rates.

Figure 17. Voltage profiles during charging at 4C rate corresponding to different porosity gradient.
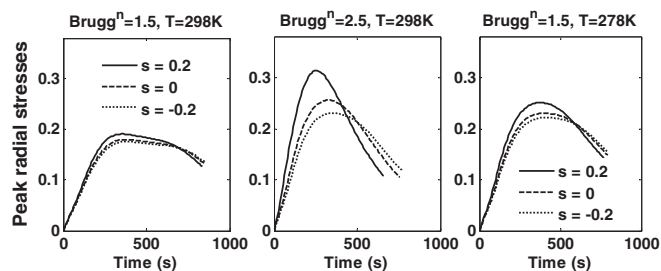

Figure 18. Peak radial stresses during charging at 4C rate at anode-separator interface.
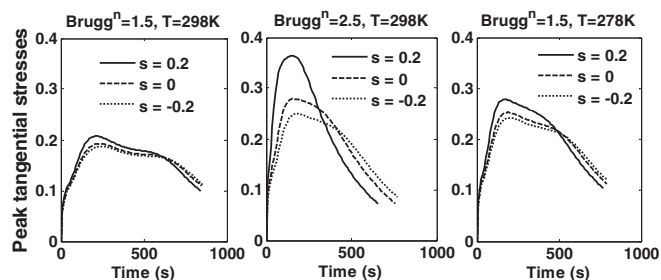

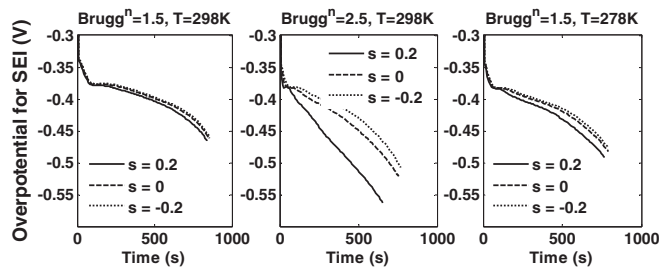**Figure 19.** Peak tangential stresses during charging at 4C rate at anode-separator interface.

Figure 20. Over-potential for SEI side reaction during charging at 4C rate.
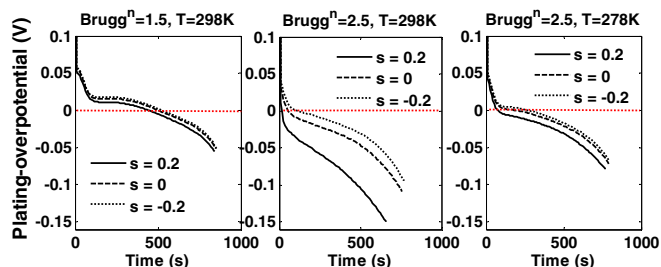

Figure 21. Over-potential for plating during charging at 4C rate.

follow similar trends in which positive slopes lead to higher magnitude of over-potential and negative slope give rise to smaller over-potential for capacity fade.

The common theme that arises from this study is that the discharge capacity is not a strong function of the length-porosity combination or porosity variation across anode for less tortuous anode at room temperature (for the specified material loading). But, for a more tortuous anode, the capacity decreases significantly at higher discharge rates. In every case, the *thinner-less porous* electrodes and electrode with less porosity at anode-separator interface leads to higher magnitude of stresses and overpotential for parasitic side reactions. For the parameters values used in the current simulation and the base case anode (0.485 porosity with 88×10^{-6} m thick electrode), the *thinner-less porous* electrode generate larger variation in current density across anode thickness compared to the *thicker-more porous* electrodes. While the trends of over-potential for SEI side reaction and plating side reaction are similar, SEI side reaction remain feasible for entire charging process, which is not the case for plating side reaction during charging.

The model used in the current study has certain limitations and shortcomings which are summarized below.

1. Simulation for high rate of discharge is performed without incorporating the diffusion limitation in the radial direction in pores.
2. The concentration dependence of the factor $(1 + d \ln f_\pm / d \ln c)$ is not taken into account.
3. The stress model used to estimate intercalation induced stresses is valid only for materials with small volume expansion. The comparison of various models for intercalation induced stresses is performed in Suthar et al.[25] for graphite material. For materials with low volumetric expansion such as graphite (with 10% volume expansion), equations given in Table III works reasonably well. For materials such as Si and Sn where volume expansion can be larger than 300%, models developed by Christensen and Newman[9] or Sikha et al.[26] can be used.
4. Overpotentials for parasitic side reactions and lithium plating reactions are approximate but this approximation should be good enough, as the magnitude of current density due to parasitic side reactions are usually very small.
5. For very few cases (especially with higher Bruggeman coefficient, low temperature and the *thinner-less porous* electrode), the lithium ion concentration in electrolyte shoots beyond the validity of the expressions for conductivity and diffusivity at the very end of discharge. Note that the expressions for conductivity and diffusivity for lithium ions in electrolyte phase comes from fitting curves to the experimental data. Hence these expressions are valid within a range for which the experiments were performed (0 to 4 mol/l in this case). Charging simulation has no such issues as the charging current is small (4C) compared to discharging currents. This effect is mainly due to concentration dependent diffusivity for lithium ion concentration in electrolyte. Such high concentration of lithium ion is not observed if concentration dependence of lithium ion in electrolyte phase is dropped.

Conclusions and Future Directions

The problem of porosity-length optimization for lithium-ion batteries is examined from a different perspective where the porosity and length are varied with a constraint of fixed theoretical capacity. First, the *thinner-less porous* and the *thicker-more porous* electrode are compared for discharge capacity, peak stresses and overpotentials for parasitic side reactions at different temperature and different Bruggeman coefficients. Low temperature charge and discharge follow trends very similar to room temperature, except for the fact that all the capacity fade effects are more pronounced and reduction in discharge capacity is more drastic at low temperature.

The Bruggeman coefficient has a significant effect on every aspect of the capacity and capacity-fade mechanisms. Smaller porosity with a larger tortuosity give rise to a significant reduction in discharge capacity despite having smaller thickness and the cell becomes more susceptible to all capacity fade mechanisms discussed in the present study.

The manufacturing difficulty of forming a uniform porosity anode is considered in a simple way where porosity is varied linearly in the anode, keeping the average porosity constant. The discharge capacity of less tortuous anode is not much affected by the porosity gradients but the capacity fade mechanics are. For the more tortuous anode ($brugg_n = 2.5$), the discharge capacities as well as capacity fade mechanisms are severely affected by a positive porosity gradient (less porosity at anode-separator interface). Interestingly a negative porosity gradient (more porosity at anode-separator interface) leads to better discharge capacity and smaller driving force for capacity fade mechanisms in all the cases. This suggests that the *thinner-less porous* electrodes may give rise to better discharge capacity and acceptable capacity fade behavior if the tortuosity is near unity (columnar electrodes).

In this study, for a fixed value of anode and cathode loading, the effect of porosity, thickness is observed at different charging/discharging conditions. The complete problem would be to derive design parameters (length, porosity and porosity distribution) for a fixed ratio of anode to cathode loading (instead of fixed value) in order to get good rate-capacities and favorable capacity fade behavior. It should be noted here that the value of the fixed ratio of anode to cathode capacity may have significant effect on the battery performance depending on the other parameter values. Such problem statement will require use of an optimization framework, as the possible design combinations are large, and will be the focus of future work.

List of Symbols

a	Surface area per volume of electrode
$brugg$	Bruggeman coefficient
c	Electrolyte concentration
c^s	Solid phase concentration
δ	Thickness of SEI layer
D	Intrinsic diffusivity of lithium ion in electrolyte
D_{eff}	Effective diffusivity of lithium ion in porous electrode
D^s	Solid phase diffusion coefficient
$E_i^{D^s}$	Activation energy (for diffusivity and reaction rate)
E_i^k	
E	Young's modulus
F	Faraday's constant
I	Applied current
j	Pore wall flux
κ	Liquid phase conductivity (intrinsic)
k	Reaction rate constant
l	Length of region
$\Re$	SEI layer resistance
R_P	Particle radius
R	Gas constant
T_{ref}	Temperature
t_+	Transference number
T_{ref}	Reference temperature (298.16 K)
T	Temperature
U	Open circuit potential
ν	Poisson's ratio
ε	Porosity
ε_f	Filling fraction
θ	State of Charge
σ	Solid phase conductivity

ρ	Density
Φ_1	Solid phase potential
Φ_2	Liquid phase potential
Ω	Partial molar volume
ξ	Scaled radial distance in anode particle $(r/R_{P,n})$

Subscripts

eff	Effective, as for diffusivity or conductivity
e	Related to electrolyte
n	Related to the negative electrode—the anode
p	Related to the positive electrode—the cathode
P	Related to particle (e.g. R_P radius of particle)
s	Related to the separator
SEI	Related to SEI

Superscripts

s	Related to Solid Phase
$+/-$	Pertains to the boundary conditions from right and left side of the interface (e.g. L_p^-, L_p^+ etc.)

References

1. C. Daniel, *JOM Journal of the Minerals, Metals and Materials Society*, **60**, 43 (2008).
2. S. M. Lukic, J. Cao, R. C. Bansal, F. Rodriguez, and A. Emadi, *Ieee Transactions on Industrial Electronics*, **55**, 2258 (2008).
3. V. Pop, H. J. Bergveld, D. Danilov, P. P. L. Regtien, and P. H. L. Notten, *Battery Management Systems: Accurate State-of-Charge Indication for Battery Powered Applications*, Springer, Dordrecht (2008).
4. J. Newman, *J. Electrochem. Soc.*, **142**, 97 (1995).
5. T. F. Fuller, M. Doyle, and J. Newman, *J. Electrochem. Soc.*, **141**, 1 (1994).
6. V. Ramadesigan, R. N. Methekar, F. Latinwo, R. D. Braatz, and V. R. Subramanian, *J. Electrochem. Soc.*, **157**, A1328 (2010).
7. Y. Ji, Y. Zhang, and C.-Y. Wang, *J. Electrochem. Soc.*, **160**, A636 (2013).
8. M. Doyle, T. F. Fuller, and J. Newman, *J. Electrochem. Soc.*, **140**, 1526 (1993).
9. J. Christensen and J. Newman, *J Solid State Electr*, **10**, 293 (2006).
10. J. Christensen and J. Newman, *J. Electrochem. Soc.*, **153**, A1019 (2006).
11. Y.-T. Cheng and M. W. Verbrugge, *J. Power Sources*, **190**, 453 (2009).
12. X. Zhang, W. Shyy, and A. Marie Sastry, *J. Electrochem. Soc.*, **154**, A910 (2007).
13. S. Renganathan, G. Sikha, S. Santhanagopalan, and R. E. White, *J. Electrochem. Soc.*, **157**, A155 (2010).
14. J.-M. Tarascon and M. Armand, *Nature*, **414**, 359 (2001).
15. P. W. C. Northrop, B. Suthar, V. Ramadesigan, S. Santhanagopalan, R. D. Braatz, and V. R. Subramanian, *J. Electrochem. Soc.*, **161**, E3149 (2014).
16. V. Zinth, C. von Lüders, M. Hofmann, J. Hattendorff, I. Buchberger, S. Erhard, J. Rebelo-Kornmeier, A. Jossen, and R. Gilles, *J. Power Sources*, **271**, 152 (2014).
17. R. D. Perkins, A. V. Randall, X. Zhang, and G. L. Plett, *J. Power Sources*, **209**, 318 (2012).
18. P. Ramadass, B. Haran, P. M. Gomadam, R. White, and B. N. Popov, *J. Electrochem. Soc.*, **151**, A196 (2004).
19. I. V. Thorat, D. E. Stephenson, N. A. Zacharias, K. Zaghib, J. N. Harb, and D. R. Wheeler, *J. Power Sources*, **188**, 592 (2009).
20. B. Vijayaraghavan, D. R. Ely, Y.-M. Chiang, R. García-García, and R. E. García, *J. Electrochem. Soc.*, **159**, A548 (2012).
21. D. Antartis, S. Dillon, and I. Chasiotis, *Journal of Composite Materials* (2015).
22. Y. H. Chen, C. W. Wang, X. Zhang, and A. M. Sastry, *J. Power Sources*, **195**, 2851 (2010).
23. N. A. Zacharias, D. R. Nevers, C. Skelton, K. Knackstedt, D. E. Stephenson, and D. R. Wheeler, *J. Electrochem. Soc.*, **160**, A306 (2013).
24. K. Takahashi and V. Srinivasan, *J. Electrochem. Soc.*, **162**, A635 (2015).
25. B. Suthar, V. Ramadesigan, S. De, R. D. Braatz, and V. R. Subramanian, *Phys. Chem. Chem. Phys.*, **16**, 277 (2014).
26. G. Sikha, S. De, and J. Gordon, *J. Power Sources*, **262**, 514 (2014).
27. V. R. Subramanian, V. Boovaragavan, V. Ramadesigan, and M. Arabandi, *J. Electrochem. Soc.*, **156**, A260 (2009).
28. J. Christensen, *J. Electrochem. Soc.*, **157**, A366 (2010).